

Application towards confocal full-field microscopic X-ray absorption near edge structure spectroscopy

Pieter Tack^{1,*}, Bart Vekemans¹, Brecht Laforce¹, Jennifer Rudloff-Grund², Willinton Y. Hernández³, Jan Garrevoet⁴, Gerald Falkenberg⁴, Frank Brenker², Pascal Van Der Voort³, Laszlo Vincze¹

¹ XMI, Department of Analytical Chemistry, Ghent University, Krijgslaan 281 S12, 9000 Ghent, Belgium

² Geoscience Institute – Mineralogy, Goethe University, Altenhöferallee 1, 60438 Frankfurt, Germany

³ Comoc, Department of Inorganic and Physical Chemistry, Ghent University, Krijgslaan 281 S3, 9000 Ghent, Belgium

⁴ Deutsch Elektronen Synchrotron DESY, Photon Sci, Notkestr 85, D-22603 Hamburg, Germany

ABSTRACT: Using X-ray absorption near edge structure spectroscopy, information on the local chemical structure and oxidation state of an element of interest can be acquired. Conventionally, this information can be obtained in a spatially resolved manner by scanning a sample through a focussed X-ray beam. Recently, full-field methods have been developed to obtain direct 2D chemical state information by imaging a large sample area. These methods are usually in transmission mode, thus restricting the use to thin and transmitting samples. Here, a fluorescence method is displayed using an energy dispersive pnCCD detector, the SLcam, characterized by measurement times far superior to what is generally applicable. Additionally, this method operates in confocal mode, thus providing direct 3D spatially resolved chemical state information from a selected subvolume of a sample, without the need of rotating a sample. The method is applied to two samples: a gold-supported on magnesia catalyst (Au/MgO) and a natural diamond containing Fe rich inclusions. Both samples provide XANES spectra that can be overlapped with reference XANES spectra, allowing this method to be used for fingerprinting and linear combination analysis of known XANES reference compounds.

Introduction

X-ray absorption near edge structure (XANES) spectroscopy imaging allows the experimentalist to extract information on the local chemical structure and oxidation state of a particular element in a sample matrix. By illuminating a sample with a focussed X-ray micro-beam and scanning the sample through this beam, spatially resolved information on the oxidation state and local chemical structure can be obtained.¹⁻⁶ However, this approach has the disadvantage that samples need to be scanned through a beam, inducing sample movement and is thus limited by the precision and accuracy of motor positioning systems. Furthermore, when 3D information is required, an additional rotation step has to be introduced as in XANES computed tomography (CT).⁷⁻⁹

In order to circumvent this time consuming methodology, it is of great interest to develop so-called full-field methodologies. In these methodologies, a large field of view is investigated in one measurement, without the need for sample movement, whilst maintaining the spatially resolved information. Initially, most full-field XANES techniques were based on transmission mode experiments¹⁰⁻¹⁵, limiting the method to thin and transmitting samples. Another method, operating in fluorescence mode and thus allowing for the investigation of thick samples, consists of fast scanning using large solid angle X-ray detectors such as the Maia.^{9,16-21} Despite the method consisting of continuous sample movement, thus inducing uncertainties with respect to measurement position and movement stability, the method is favoured due to its impressively fast acquisition rates (order of a few ms/point/energy).

Another option for spatially resolved fluorescence mode XANES arises with the use of full-field methodology based on energy dispersive CCD based detectors, such as the SLcam.^{22,23} The proof of principle for XANES using this device has been reported previously.²⁴ In this work, the method has been expanded to extract depth selective information by applying a confocal detection scheme, analogous to earlier X-ray fluorescence spectroscopy experiments performed with this detector^{25,26}; a virtual slice of the sample is illuminated using a focussed thin sheet beam, a part of which is selectively monitored by overlapping the sheet beam with the focal field of view of the detector, equipped with a polycapillary optic. By moving the sample through the sheet beam, making use of a single translation motor, and performing a monochromator energy scan at each position, 3D resolved XANES data is obtained. Here this method is applied to two samples: a) a Au/MgO catalyst particle which can be applied to several (photosensitive) catalytic processes (e.g. oxidation reactions²⁷⁻²⁹, hydrogenation reactions³⁰ and C-C coupling processes³¹) in which the local charge or oxidation state of Au has an important influence on the catalytic efficiency and sensitivity³²⁻³⁷ and b) a natural alluvial diamond from the Juina area, Mato Grosso, Brazil which may have an ultra deep origin as shown for many samples of the same location.³⁸⁻⁴⁰ The diamond contains inclusions which have their stability field at least within the transition zone (410-670 km depth) and thus represent some of the only samples providing direct information on the materials from deep Earth.³⁹⁻⁴¹

It is shown that the applied depth selective method, although still time consuming, is vastly superior in speed compared to

other currently applied XANES methodologies and is feasible to perform during a standard measuring campaign allocated at a synchrotron radiation facility. Additionally, a method is discussed to facilitate handling and processing of the large amount of created data, using a combination of principal component analysis (PCA) and K-means clustering. The obtained XANES spectra can be overlapped with the spectra of reference compounds measured in transmission mode, proving the method allows for fingerprinting and linear combination data processing approaches.

Materials and Methods

SLcam. The SLcam, or “colour X-ray camera” developed by PNSensor GmbH (Munich, Germany) and the Institute for Scientific Instruments GmbH (IFG, Berlin, Germany), is an energy dispersive pnCCD detector consisting of 264×264 pixels of 48×48 μm^2 size, on a 450 μm thick backside illuminated Si detector crystal rendering it highly sensitive to X-rays in the 3–20 keV range.^{22,23} In these experiments, the detector was equipped with a 6:1 magnifying polycapillary optic, resulting in an effective spatial resolution of 8×8 μm^2 and a field of view of approximately 2×2 mm². The chip is read out through a split dark frame storage mode where each half of the chip is read out by 2 CAMEX modules, effectively splitting the detector chip readout in four quadrants. Each frame is read out in 2.5 ms, resulting in a 400 Hz readout frequency in which a full X-ray fluorescence (XRF) spectrum (0–20 keV) is acquired for each pixel (69696 spectra/frame).

These XRF spectra were then further processed using the AXIL software package to extract the fluorescent line intensities.⁴²

Micro-CT. As a pre-characterization step, transmission X-ray computed tomography (CT) were performed on a laboratory instrument, details of which are described elsewhere.⁴³ The X-ray source, a W anode X-ray tube (XrayWorX GmbH, Garbsen, Germany) was operated at 70 kV voltage and 3 W power. The transmission signal was detected by a 20 MHz readout frequency VHR CCD camera (Photonic Science Ltd., Mountfield, UK) consisting of 4008×2672 9×9 μm^2 pixels and a Gd₂OS:Tb scintillator screen. A 360° rotation was performed in 1501 steps with an exposure time of 1 s/rotation. Two consecutive measurements were performed at different sample heights in order to cover the full particle size. The data was backwards projected to obtain virtual slices of the sample, which were visualised using the Drishti software package⁴⁴.

XANES. XANES experiments were performed at beamline P-06 at the PETRA III synchrotron facility at DESY (Hamburg, Germany). The undulator generated primary X-ray beam was rendered monochromatic using a Si(111) double crystal monochromator, providing an energy resolution dE/E of approximately $1.4 \cdot 10^{-4}$. The second mirror of a Kirkpatrick-Baez (KB) mirror system was used to focus the beam to a vertically oriented sheet beam of approximately 1.8×0.007 (V×H) mm², with a horizontal divergence of approximately 2 mrad. No change in sheet beam position was observed by scanning through the primary X-ray beam energy.

Au L₃-edge (E_0 : 11.919 keV) and Fe K-edge (E_0 : 7.112 keV) XANES data were collected monitoring the excitation energy dependent X-ray fluorescence emission using the SLcam. Au L₃-edge XANES consisted of energy scans from 11.808 keV to 11.908 keV in 5 eV steps (5 min/step acquisition), 11.909 keV to 11.938 keV in 1 eV steps and from 11.941 keV to 12.079 keV in 3 eV steps (10 min/step acquisition);

adding up to 98 energy steps. Fe K-edge XANES were performed by energy scans from 7.087 keV to 7.117 keV in 5 eV steps (9 min/step acquisition), 7.118 keV to 7.145 keV in 1 eV steps (18 min/step acquisition) and from 7.146 keV to 7.173 keV in 3 eV steps (18 min/step acquisition). Reference spectra were obtained from pure compounds (AuCN, Au foil, Fe foil), measured in transmission mode.

XANES spectra were normalised by subtracting the pre-edge background and fitting the post-edge region to a linear function, which was then normalised to 1 at E_0+50 eV.

Samples. A Au/MgO catalyst (having 1.0 wt% of Au) was prepared by a modified deposition-precipitation method described elsewhere⁴⁵, using HAuCl₄ (Union Chimique Belge) as a gold precursor, urea (Sigma-Aldrich) as a precipitation agent and a meso-macroporous MgO support (prepared via a hydrothermal synthesis method adapted from Rezaei *et al.*⁴⁶). A sintering step at 500 °C was performed in order to increase the Au particle sizes closer to the microscopic range, providing a more suitable size given the spatial resolution of the described technique (~8 μm resolution). The synthesized powder was then pressed to a pellet under a pressure of 300–400 bar for 5 minutes. A piece of suitable size (~2×2 mm²) was cut from the pellet and attached to a graphite pin using clear liquid Patex glue.

A second sample consists of a diamond from São Luiz placer diamond deposit in Juina, Mato Grosso, Brazil (SL FFM 08), containing Fe-rich inclusions from possible deep Earth sources. Juina provides large amount of so-called ultra-deep diamonds which were formed within ultra-deep parts of the Earth – the asthenospheric upper mantle (<410 km), the transition zone (410–670 km) or even the lower mantle (>670 km).^{38,40,47–50} Once the materials are encapsulated, the inclusions remain chemically unchanged during exhumation due to the inert and stable nature of the host diamond.⁴⁰ Preliminary Raman investigation of diamond SL FFM 08 revealed the presence of walstromite and walstromite+CaTi-ferrovskite among other phases.

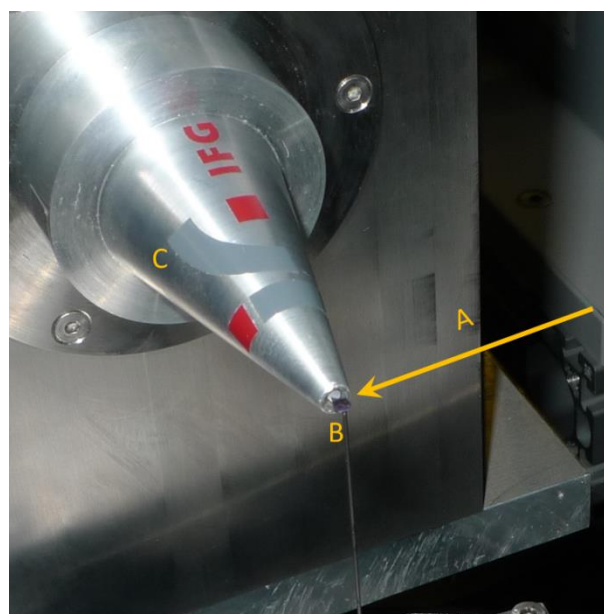


Figure 1: Photograph of the setup displaying the direction of primary X-ray sheet beam (A), the Au/MgO catalyst particle sample positioned on a XYZ translation and rotation stage (B) and the SLcam with 6:1 magnifying polycapillary optic (C).

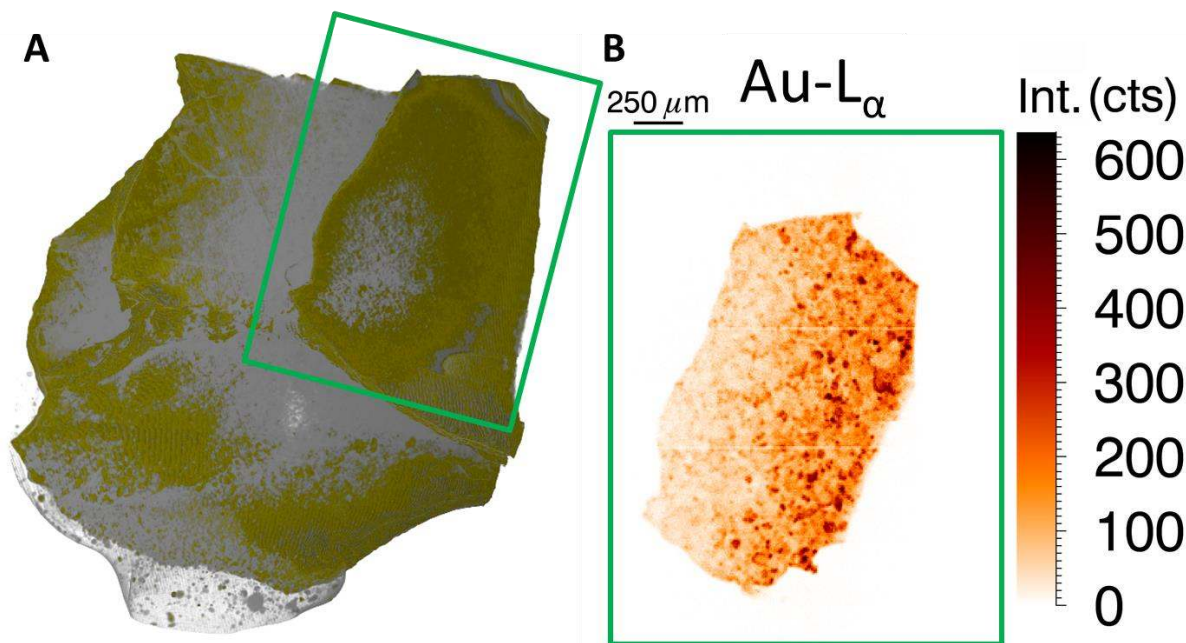


Figure 2: A) Transmission tomography rendered volume of a Au/MgO catalyst particle with gray parts representing the catalyst particle and gold/yellow parts representing the Au nanoparticles distributed through the volume. B) The full-field confocal Au- L_{α} XRF emission of the region marked in green. (E_0 : 12.079 keV, t_m : 10 min).

Results and Discussion

The SLcam was placed perpendicular to the primary X-ray beam under a 90 degree scattering geometry, in the plane of polarisation of the synchrotron ring (Figure 1). This effectively minimizes X-ray scattering by the sample to impinge on the detector; an important feature considering the low atomic number (Z) matrix of the investigated samples. A virtual slice of the sample was illuminated using the vertically focussed sheet beam and the SLcam field of view was co-aligned with the illuminated sample area, thus creating a confocal volume from which information is selectively acquired in an analogous manner to the confocal full-field XRF scheme as presented by Radtke *et al.* and Garrevoet *et al.*^{25,26}

By scanning over the energy of the primary X-ray beam and detecting the emitted fluorescence from the illuminated cross-section by the SLcam detector for each energy step, direct 3D X-ray absorption spectroscopy data is acquired. Considering the limited count rate of the SLcam (approximately 10 counts/s/pixel) and low detected flux due to the low transmission efficiency of the applied polycapillary optic, seemingly long acquisition times per energy step have to be applied (5-20 minutes/energy). However, one should realise this acquisition represents 20 minutes for a total of $69696 \times 8 \times 8 \mu\text{m}^2$ pixels: the equivalent of 17 ms/point/energy. This is a count rate far superior to what is usually applied in confocal measurements^{3,6,51-55}, and very competitive to standard 3D XANES methodologies based on, for instance, tomographic reconstruction.

A Au/MgO catalyst particle was investigated in order to determine the spatially resolved chemical state of Au, as this can have a great effect on the catalytic activity of the particles.³²⁻³⁷ As such, it is important to know whether a used reduction step during the synthesis affected only the outer Au particles, or whether the reduction also occurred inside the catalyst material. Using the applied methodology, this question can be answered.

An initial transmission tomography experiment was performed on the catalyst particle in order to obtain a rough overview of the Au particle distribution inside the catalyst (Figure 2A). It is clear this method does not provide information on the local chemical structure of the Au particles, as it mainly displays differences in local density. It is however a useful method to obtain a full 3D “roadmap” of the catalyst particle in a fairly short time, which allows for straightforward recognition of the investigated volumes during the confocal full-field experiments based on the emitted fluorescence and scattering radiation. The XRF Au- L_{α} intensity of the full-field XANES investigated area is compared to the transmission CT data in Figure 2B. The intensity gradient in the XRF data is explained by the absorption of the primary X-ray beam in the sample, as well as differences in sample thickness the emitted fluorescence radiation travels through (Web Enhanced Object movie). As such, the region that contains a similar Au concentration based on the transmission CT seems less concentrated based on the XRF data. This reduction in primary beam intensity is not problematic for the full-field XANES experiments however, as sufficient XRF intensity was detected over the entire illuminated sample region.

A major issue in full-field XANES spectroscopy concerns the handling of the large amount of data. Considering this experiment, for each energy step 69696 XRF spectra were generated. Multiply this by 98 energy steps (as for our Au L_3 -edge XANES scan) and 2 sample positions in order to cover the entire sample cross section, one obtains over 13 million XRF spectra. Each of these spectra was processed to determine the relevant peak intensities, resulting in nearly 140000 XANES spectra. It is clear that this amount of spectra does not lend itself to the task of normalising and processing each spectrum manually. As such, a sequence of principal component analysis (PCA) and K-means clustering was performed in order to group and average XANES spectra with similar

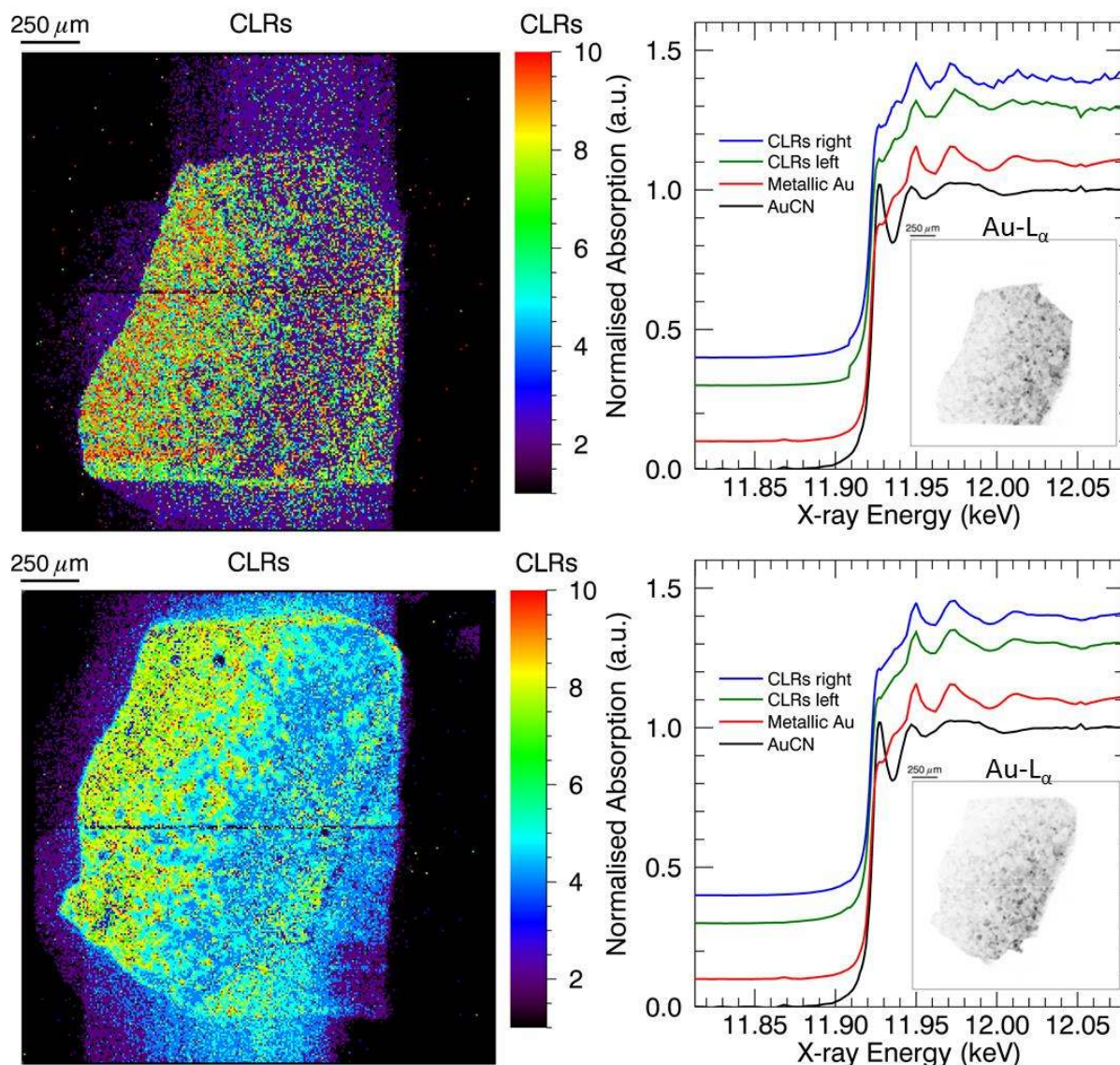


Figure 3: K-means clustering on PCA scores result (left) and corresponding Au L_3 -edge XANES spectra for two large groups of clusters (CLRs) (right) for a Au/MgO catalyst particle, along with the spectra of reference compounds. An inset XRF Au distribution image is shown for each region. ‘CLRs right’ corresponds to the clusters on the right side of the particle, whereas ‘CLRs left’ corresponds to the clusters on the left side of the particle as displayed on the PCA score results.

variations as a function of energy. During the initial steps of the in-house developed PCA analysis routine, a rough XANES normalisation is performed by fitting the pre-edge and post-edge regions by a linear function each. The pre-edge region is then normalised to 0, whereas the post-edge region is normalised to 1. This pre-normalisation effectively reduces concentration effects that would otherwise cause the PCA to simply group spectra of similar intensity/edge jump.

Furthermore, voxels downstream in the sample are excited by a primary beam whose intensity has been energy dependently modified due to the energy dependent absorption by the sample upstream of the primary X-ray beam, that is the primary beam intensity illuminating the Au particles downstream is a product of the initial primary beam intensity and the attenuation of the X-rays by Au particles upstream.^{3,56} This effect is more pronounced as higher concentrations of the element over which edge is scanned are present in the sample. To correct for this, the Au- L_{α} and Fe- K_{α} intensities for each sepa-

rate voxel were divided by the corresponding total intensity of energies lower than these XRF lines (I_{lowE}). This method essentially provides an I_0 normalisation on a point-by-point base that is independent of the absorption of the primary beam modulated by interactions occurring more upstream. In this particular case however, this normalisation was only used before the PCA and K-means clustering as I_{lowE} on a point-by-point basis suffered from poor counting statistics. Despite normalising for I_{lowE} providing clusters that correspond better with expected distributions based on for instance transmission CT experiments, using I_{lowE} to normalise the final XANES spectra resulted in the disadvantageous addition of noise. As such, it was opted here to normalise the final (represented) XANES spectra using the general I_0 as registered by an ion chamber upstream of the KB mirror system, thus normalising each point in the full-field slice for the same value of I_0 . In each case however the obtained XANES spectra had identical edge positions and XANES structure (within noise) when

normalising with I_0 or I_{lowE} , thus proving both normalisation methods are viable in this case. A flowchart of the data processing structure that was followed is visualised in Figure S1 in Supporting Information.

The results of clustering and the resulting extracted XANES profiles for the Au/MgO particle are shown in Figure 3. It is clear the clustering splits the Au/MgO in two large regions: the left and right region, where the left region is characterized by lower Au- L_{α} intensity (Figure 2) and the right region represents the more intense Au- L_{α} regions. In both cases, the extracted XANES spectra corresponding to these clusters show nearly identical XANES curves, which are in turn nearly identical to the reference spectrum of metallic Au. Only a very slight contribution of Au^+ can be seen at ~ 11.928 keV, an interesting feature as the presence of a positive charge is advantageous for certain catalytic reactions, depending on the involved chemistry, such as the catalytic conversion of CO to CO_2 as is performed in air purification processes.³²⁻³⁷

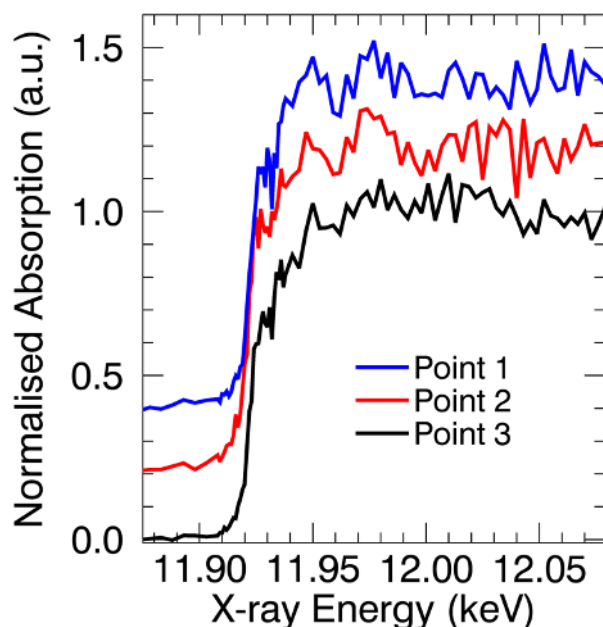


Figure 4: Single voxel Au L_3 -edge XANES spectra for three randomly selected voxels in the Au/MgO sample data set. Noise levels are fairly high in the post-edge region, but a clear edge position is distinguishable.

The single voxel XANES spectra of three randomly selected voxels are displayed in Figure 4. It is clear that significant noise levels are present in the post-edge region of the spectra, which complicated the performed PCA routine. Nevertheless, the main absorption edge is clearly visible and the general trend of the characteristic metallic Au features at approximately 11.95 and 11.97 keV can be differentiated slightly as well, showing the PCA is sufficiently sensitive in order to differentiate between compounds containing different oxidation states of the element of interest.

From the XRF data set it is also clear that in nearly the entire Au/MgO catalyst particle, Au particles are to be found. However, some regions are locally enriched in Au particles, characterised by the Au- L_{α} XRF hotspots (Figure 2B). Nevertheless, all particles are of mainly metallic Au (Au^0) with perhaps a small charge.

A second sample, a natural deep Earth diamond containing Fe rich inclusions, was investigated. This sample profits sig-

nificantly from the confocal detection scheme, that is inherent to the full-field XANES methodology using the SLcam, as the diamond carbon matrix has a high Compton scattering cross section. In traditional detection schemes (e.g. XANES tomography) the scattering induced by the diamond would be sufficient to even overload most common fluorescence detectors, significantly reducing signal-to-scatter ratios achievable by the experiment. By applying the confocal method however, most of the scattering by the carbon matrix can be suppressed due to the restricted scattering volume combined with the 90 degree detection angle. The results of the clustering, obtained using an analogous procedure as described above, and the resulting XANES spectra are displayed in Figure 5. Again it appears all the Fe in the inclusions has the same or very similar chemical signature, which is according to expectation for this particular specimen. The obtained XANES curve is very similar to that of a magnetite Fe_3O_4 reference compound, allowing us to deduce that the Fe in the investigated diamond inclusion consists of a mixture of Fe^{2+} and Fe^{3+} ions ordered in a magnetite-like structure. It should be noted that the pre-edge peak at ~ 7.115 keV, visible for pure Fe_3O_4 , is not visible in the confocal full-field XANES spectrum. This is either because the Fe surrounding inside the diamond inclusion, in contrast to magnetite, is characterized by an inversion symmetry (e.g. octahedral surrounding) or because the counting statistics in this energy region of the spectrum were insufficient to detect any pre-edge features. Additionally, the features around ~ 7.146 keV are missing from the full-field XANES spectrum as well. This is unlikely due to poor counting statistics as the corresponding peak in the Fe_3O_4 spectrum is larger than the noise fluctuations visible in the full-field spectrum. This further strengthens the hypothesis that the Fe surrounding inside the diamond inclusions is similar but not identical to pure magnetite.

Conclusion

A confocal full-field XANES experiment was performed by illuminating a sample with a thin sheet beam, and selectively detecting the emitted fluorescence radiation as a function of primary X-ray beam energy in a spatially resolved manner using an energy dispersive pnCCD detector, the SLcam, characterized by a 2×2 mm² field of view with 8 μm spatial resolution. Despite the seemingly long measurement times (12-15 hours/XANES scan consisting of 98 energy points) this depth sensitive methodology is revolutionary fast considering the large field of view and amount of simultaneously monitored voxels (69696). In comparison, to perform a similar XANES scan on a point-by-point scanning regime, each XANES scan should take only 750 ms/point including motor movement overhead time, which becomes significant at such movement rates.

Furthermore, as this technique is confocal in nature, it is possible to extract depth resolved 2D information from a virtual slice in a sample without the requirement of rotating or otherwise moving the sample during measurement. Additionally, full 3D chemical state information can in principle be acquired by extending the described method by a lateral movement of the sample through the sheet beam, along the normal of the detector chip surface and performing an energy scan at each sample position.

In order to be able to handle the large amount of data acquired during this methodology, a clustering method based on PCA and K-means clustering was proposed in order to group

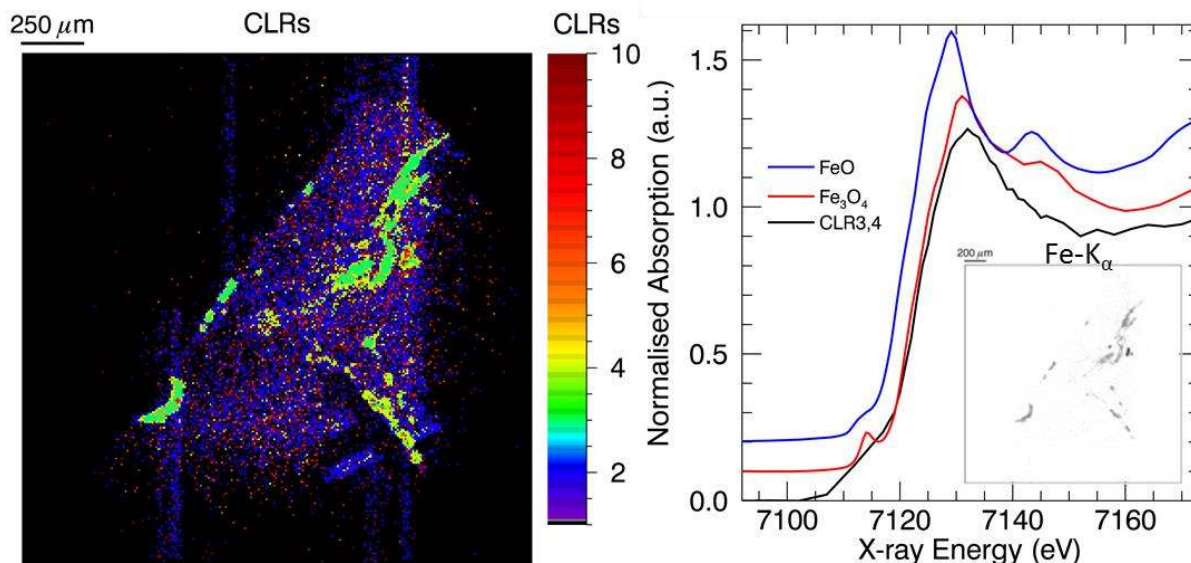


Figure 5: K-means clustering on PCA scores result (left) and corresponding Fe K-edge XANES spectra for two large groups of clusters (right) for a natural diamond with Fe containing deep Earth inclusions, along with the spectra of reference compounds. An inset XRF Fe distribution image is shown for the investigated subvolume.

similar XANES profiles, providing a semi-automated way of data reduction.

The methodology was applied to two samples: a) a Au/MgO catalyst sample in which the spatial chemical state distribution of the Au particles was monitored as this can have an impact catalytic activity, as well as b) a natural diamond containing Fe-rich inclusions, in which the chemical state of the Fe can give information on the redox conditions of the Earth's interior and as such can have great implications towards the understanding of our planet. In both cases the method resulted in XANES spectra which showed great agreement to reference compound spectra obtained in transmission mode.

Future improvements to this method are expected to be made mainly in the development of new X-ray guiding optics, providing a higher transmission efficiency and better spatial resolution. Additionally, new technologies could also result in obtaining faster detector readout and larger fields of view whilst maintaining similar or even better spatial resolution.

ASSOCIATED CONTENT

Supporting Information

The Supporting Information is available free of charge on the ACS Publications website.

Data processing sequence flow chart

X-ray transmission tomography video displaying measured confocal volume (WMV)

AUTHOR INFORMATION

Corresponding Author

* Pieter.Tack@UGent.be, Department of Analytical Chemistry, Ghent University, Krijgslaan 281 S12, 9000 Ghent, Belgium.

Author Contributions

The manuscript was written through contributions of all authors. All authors have given approval to the final version of the manuscript.

ACKNOWLEDGMENT

P.T. and B.L. are funded by a PhD grant of the Agency for Innovation by Science and Technology (IWT). The authors wish to thank the P-06 staff for their help and support during the experiments

REFERENCES

- (1) Tack, P.; Cotte, M.; Bauters, S.; Brun, E.; Banerjee, D.; Bras, W.; Ferrero, C.; Delattre, D.; Mocella, V.; Vincze, L. *Scientific Reports* **2016**, *6*, 20763.
- (2) Mino, L.; Borfecchia, E.; Groppo, C.; Castelli, D.; Martinez-Criado, G.; Spiess, R.; Lamberti, C. *Catal. Today* **2014**, *229*, 72-79.
- (3) Luhl, L.; Hesse, B.; Mantouvalou, I.; Wilke, M.; Mahlkow, S.; Aloupi-Siotis, E.; Kanngiesser, B. *Anal. Chem.* **2014**, *86*, 6924-6930.
- (4) Terzano, R.; Mimmo, T.; Vekemans, B.; Vincze, L.; Falkenberg, G.; Tomasi, N.; Schnell Ramos, M.; Pinton, R.; Cesco, S. *Analytical and bioanalytical chemistry* **2013**, *405*, 5411-5419.
- (5) Terabayashi, M.; Matsui, T.; Okamoto, K.; Ozawa, H.; Kaneko, Y.; Maruyama, S. *Island Arc* **2013**, *22*, 37-50.
- (6) Tack, P.; Bauters, S.; Mauro, J. C.; Smedskjaer, M. M.; Vekemans, B.; Banerjee, D.; Bras, W.; Vincze, L. *RSC Adv.* **2016**, *6*, 24060-24065.
- (7) Rau, C.; Somogyi, A.; Simionovici, A. *Nuclear Instruments & Methods in Physics Research Section B-Beam Interactions with Materials and Atoms* **2003**, *200*, 444-450.
- (8) Rau, C.; Somogyi, A.; Bytchkov, A.; Simionovici, A. *Proceedings of SPIE* **2002**, *4503*, 249-255.
- (9) Ryan, C. G.; Siddons, D. P.; Kirkham, R.; Li, Z. Y.; de Jonge, M. D.; Paterson, D. J.; Kuczewski, A.; Howard, D. L.; Dunn, P. A.; Falkenberg, G.; Boesenberg, U.; De Geronimo, G.; Fisher, L. A.; Halfpenny, A.; Lintern, M. J.; Lombi, E.; Dyl, K. A.; Jensen, M.; Moorhead, G. F.; Cleverley, J. S.; Hough, R. M.; Godel, B.; Barnes, S. J.; James, S. A.; Spiers, K. M.; Alfeld, M.; Wellenreuther, G.; Vukmanovic, Z.; Borg, S. *J Phys Conf Ser* **2014**, *499*, 012002.
- (10) Nelson, G. J.; Harris, W. M.; Izzo, J. R.; Grew, K. N.; Chiu, W. K. S.; Chu, Y. S.; Yi, J.; Andrews, J. C.; Liu, Y.; Pianetta, P. *Appl. Phys. Lett.* **2011**, *98*, 173109.
- (11) Meirer, F.; Cabana, J.; Liu, Y.; Mehta, A.; Andrews, J. C.; Pianetta, P. *Journal of synchrotron radiation* **2011**, *18*, 773-781.
- (12) Andrews, J. C.; Meirer, F.; Liu, Y.; Mester, Z.; Pianetta, P. *Microsc. Res. Tech.* **2011**, *74*, 671-681.

- (13) Meirer, F.; Liu, Y.; Pouyet, E.; Fayard, B.; Cotte, M.; Sanchez, C.; Andrews, J. C.; Mehta, A.; Sciau, P. *J. Anal. At. Spectrom.* **2013**, *28*, 1870.
- (14) Fayard, B.; Pouyet, E.; Berruyer, G.; Bugnazet, D.; Cornu, C.; Cotte, M.; Andrade, V. D.; Chiaro, F. D.; Hignette, O.; Kieffer, J.; Martin, T.; Papillon, E.; Salomé, M.; Sole, V. A. *J Phys Conf Ser.* **2013**, *425*, 192001.
- (15) Mangold, S.; Steininger, R.; Rolo, T. d. S.; Göttlicher, J. *J Phys Conf Ser.* **2013**, *430*, 012130.
- (16) Kopittke, P. M.; de Jonge, M. D.; Wang, P.; McKenna, B. A.; Lombi, E.; Paterson, D. J.; Howard, D. L.; James, S. A.; Spiers, K. M.; Ryan, C. G.; Johnson, A. A.; Menzies, N. W. *The New phytologist* **2014**, *201*, 1251-1262.
- (17) Monico, L.; Janssens, K.; Alfeld, M.; Cotte, M.; Vanmeert, F.; Ryan, C. G.; Falkenberg, G.; Howard, D. L.; Brunetti, B. G.; Miliani, C. *J. Anal. At. Spectrom.* **2015**, *30*, 613.
- (18) Howard, D. L.; de Jonge, M. D.; Lau, D.; Hay, D.; Varcoe-Cocks, M.; Ryan, C. G.; Kirkham, R.; Moorhead, G.; Paterson, D.; Thurrowgood, D. *Anal. Chem.* **2012**, *84*, 3278-3286.
- (19) Ryan, C. G.; Kirkham, R.; Hough, R. M.; Moorhead, G.; Siddons, D. P.; de Jonge, M. D.; Paterson, D. J.; De Geronimo, G.; Howard, D. L.; Cleverley, J. S. *Nuclear Instruments & Methods in Physics Research Section a-Accelerators Spectrometers Detectors and Associated Equipment* **2010**, *619*, 37-43.
- (20) Kirkham, R.; Dunn, P. A.; Kuczewski, A. J.; Siddons, D. P.; Dodanwala, R.; Moorhead, G. F.; Ryan, C. G.; Geronimo, G. D.; Beuttenmuller, R.; Pinelli, D.; Pfeffer, M.; Davey, P.; Jensen, M.; Paterson, D. J.; Jonge, M. D. d.; Howard, D. L.; Küsel, M.; McKinlay, J. In *The 10th International Conference on Synchrotron Radiation Instrumentation*; American Institute of Physics, 2010, pp 240-243.
- (21) Etschmann, B. E.; Ryan, C. G.; Brugger, J.; Kirkham, R.; Hough, R. M.; Moorhead, G.; Siddons, D. P.; De Geronimo, G.; Kuczewski, A.; Dunn, P.; Paterson, D.; de Jonge, M. D.; Howard, D. L.; Davey, P.; Jensen, M. *Am. Mineral.* **2010**, *95*, 884-887.
- (22) Ordavo, I.; Ihle, S.; Arkadiev, V.; Scharf, O. *Nuclear Instruments and Methods in Physics Research A* **2010**, doi:10.1016/j.nima.2011.05.080.
- (23) Scharf, O.; Ihle, S.; Ordavo, I.; Arkadiev, V.; Bjeoumikhov, A.; Bjeoumikhova, S.; Buzanich, G.; Gubzhokov, R.; Gunther, A.; Hartmann, R.; Kuhbacher, M.; Lang, M.; Langhoff, N.; Liebel, A.; Radtke, M.; Reinholz, U.; Riesemeier, H.; Soltan, H.; Struder, L.; Thunemann, A. F.; Wedell, R. *Anal. Chem.* **2011**, *83*, 2532-2538.
- (24) Tack, P.; Garrevoet, J.; Bauters, S.; Vekemans, B.; Laforce, B.; Van Ranst, E.; Banerjee, D.; Longo, A.; Bras, W.; Vincze, L. *Anal. Chem.* **2014**, *86*, 8791-8797.
- (25) Radtke, M.; Buzanich, G.; Curado, J.; Reinholz, U.; Riesemeier, H.; Scharf, O. *J. Anal. At. Spectrom.* **2014**, *29*, 1339-1344.
- (26) Garrevoet, J.; Vekemans, B.; Tack, P.; De Samber, B.; Schmitz, S.; Brenker, F. E.; Falkenberg, G.; Vincze, L. *Anal. Chem.* **2014**, *86*, 11826-11832.
- (27) Wang, Z.; Xu, C. L.; Wang, H. F. *Catal. Lett.* **2014**, *144*, 1919-1929.
- (28) Wang, L.; Yang, D.; Wang, J.; Zhu, Z. B.; Zhou, K. B. *Catal. Commun.* **2013**, *36*, 38-42.
- (29) Jia, C. J.; Liu, Y.; Bongard, H.; Schuth, F. *J. Am. Chem. Soc.* **2010**, *132*, 1520-1522.
- (30) Guzman, J.; Gates, B. C. *J. Catal.* **2004**, *226*, 111-119.
- (31) Hammond, C.; Lopez-Sanchez, J. A.; Ab Rahim, M. H.; Dimitratos, N.; Jenkins, R. L.; Carley, A. F.; He, Q.; Kiely, C. J.; Knight, D. W.; Hutchings, G. J. *Dalton transactions* **2011**, *40*, 3927-3937.
- (32) Rodriguez, J. A.; Si, R.; Evans, J.; Xu, W.; Hanson, J. C.; Tao, J.; Zhu, Y. *Catal. Today* **2015**, *240*, 229-235.
- (33) Meire, M.; Tack, P.; De Keukeleere, K.; Balcaen, L.; Pollefeyt, G.; Vanhaecke, F.; Vincze, L.; Van Der Voort, P.; Van Driessche, I.; Lommens, P. *Spectrochim Acta B* **2015**, *110*, 45-50.
- (34) Zamponi, F.; Penfold, T. J.; Nachtegaal, M.; Lubcke, A.; Rittmann, J.; Milne, C. J.; Chergui, M.; van Bokhoven, J. A. *Phys. Chem. Chem. Phys.* **2014**, *16*, 23157-23163.
- (35) Pacchioni, G. *Phys. Chem. Chem. Phys.* **2013**, *15*, 1737-1757.
- (36) Zhang, C.; Michaelides, A.; Jenkins, S. J. *Phys. Chem. Chem. Phys.* **2011**, *13*, 22-33.
- (37) Zhang, C.; Michaelides, A.; King, D. A.; Jenkins, S. J. *J. Am. Chem. Soc.* **2010**, *132*, 2175-2182.
- (38) Kaminsky, F. V.; Zakharchenko, O. D.; Davies, R.; Griffin, W. L.; Khachatryan-Blinova, G. K.; Shiryaev, A. A. *Contrib. Mineral. Petrol.* **2001**, *140*, 734-753.
- (39) Brenker, F. E.; Vollmer, C.; Vincze, L.; Vekemans, B.; Szymanski, A.; Janssens, K.; Szaloki, I.; Nasdala, L.; Joswig, W.; Kaminsky, F. *Earth. Planet. Sci. Lett.* **2007**, *260*, 1-9.
- (40) Pearson, D. G.; Brenker, F. E.; Nestola, F.; McNeill, J.; Nasdala, L.; Hutchison, M. T.; Matveev, S.; Mather, K.; Silversmit, G.; Schmitz, S.; Vekemans, B.; Vincze, L. *Nature* **2014**, *507*, 221-224.
- (41) Kaminsky, F. *Earth-Science Reviews* **2012**, *110*, 127-147.
- (42) Vekemans, B.; Janssens, K.; Vincze, L.; Adams, F.; Vanespen, P. *X-Ray Spectrom.* **1994**, *23*, 278-285.
- (43) Laforce, B.; Vermeulen, B.; Garrevoet, J.; Vekemans, B.; Hoorebeke, L. V.; Janssen, C.; Vincze, L. *Anal. Chem.* **2016**, *88*, 3386-3391.
- (44) Ajay Limaye, D. *Vis Baltimore* **2006**.
- (45) Estrada, M.; Costa, V. V.; Beloshapkin, S.; Fuentes, S.; Stoyanov, E.; Gusevskaya, E. V.; Simakov, A. *Appl Catal a-Gen* **2014**, *473*, 96-103.
- (46) Rezaei, M.; Khajenoori, M.; Nematollahi, B. *Mater. Res. Bull.* **2011**, *46*, 1632-1637.
- (47) Harte, B.; Harris, J. W.; Hutchison, M. T.; Watt, G. R.; Wilding, M. C. *Geochemical Society* **1999**, *6*, 125-153.
- (48) Brenker, F. E.; Vincze, L.; Vekemans, B.; Nasdala, L.; Stachel, T.; Vollmer, C.; Kersten, M.; Somogyi, A.; Adams, F.; Joswig, W.; Harris, J. W. *Earth. Planet. Sci. Lett.* **2005**, *236*, 579-587.
- (49) Hayman, P. C.; Kopylova, M. G.; Kaminsky, F. V. *Contrib. Mineral. Petrol.* **2005**, *149*, 430-445.
- (50) B., H.; J.W., H. *Mineralogical Magazine* **1994**, *58A*, 384-385.
- (51) Laclavetine, K.; Ager, F. J.; Arquillo, J.; Respaldiza, M. Á.; Scrivano, S. *Microchem. J.* **2016**, *125*, 62-68.
- (52) Luhl, L.; Mantouvalou, I.; Schaumann, I.; Vogt, C.; Kanngiesser, B. *Anal. Chem.* **2013**, *85*, 3682-3689.
- (53) Silversmit, G.; Vekemans, B.; Appel, K.; Schmitz, S.; Schoonjans, T.; Brenker, F. E.; Kaminsky, F.; Vincze, L. *Anal. Chem.* **2011**, *83*, 6294-6299.
- (54) Kanngießner, B.; Malzer, W.; Mantouvalou, I.; Sokaras, D.; Karydas, A. G. *Appl. Phys. A* **2011**, *106*, 325-338.
- (55) Silversmit, G.; Vekemans, B.; T. Schoonjans; Voorde, L. V. D.; Schmitz, S.; Appel, K.; Brenker, F. E.; Vincze, L. *Photon Science 2009 : highlights and HASYLAB annual report : author contributions* **2010**.
- (56) Luhl, L.; Mantouvalou, I.; Malzer, W.; Schaumann, I.; Vogt, C.; Hahn, O.; Kanngiesser, B. *Anal. Chem.* **2012**, *84*, 1907-1914.

Authors are required to submit a graphic entry for the Table of Contents (TOC) that, in conjunction with the manuscript title, should give the reader a representative idea of one of the following: A key structure, reaction, equation, concept, or theorem, etc., that is discussed in the manuscript. Consult the journal's Instructions for Authors for TOC graphic specifications.

Insert Table of Contents artwork here

